Astronomy & Astrophysics manuscript no. octupole_287869463_aa_v20
March 8, 2026

Discovery of the First Octupole Pulsation Mode in a δ Scuti Star

A Stationary $\ell = 3$ Sectoral Mode

S. A. Rappaport[1,2], R. Jayaraman[3], G. Handler[4], D. Kurtz[5,6], V. Zhang[7], R. Gagliano[8], B. Powell[9], J. Fuller[10], T. Borkovits[1,11,12,13,14], V. Kostov[9,15], and J. Daszyńska-Daszkiewicz[16,17]

[1] HUN–REN–SZTE Stellar Astrophysics Research Group, H-6500 Baja, Szegedi út, Kt. 766, Hungary
[2] Department of Physics, Kavli Institute for Astrophysics and Space Research, M.I.T., Cambridge, MA 02139, USA
e-mail: sar@mit.edu
[3] Department of Astronomy, Cornell University, 122 Sciences Dr, Ithaca, NY 14850 USA
[4] Nicolaus Copernicus Astronomical Center, Polish Academy of Sciences, ul. Bartycka 18, PL-00-716 Warszawa, Poland
[5] Centre for Space Research, North-West University, Mahikeng 2745, South Africa
[6] Jeremiah Horrocks Institute, University of Lancashire, Preston PR1 2HE, UK
[7] Harvard University, Cambridge, MA 02138, USA
[8] Amateur Astronomer, Glendale, AZ 85308
[9] NASA Goddard Space Flight Center, 8800 Greenbelt Road, Greenbelt, MD 20771, USA
[10] TAPIR, Mailcode 350-17, California Institute of Technology, Pasadena, CA 91125, USA
[11] Baja Astronomical Observatory of University of Szeged, H-6500 Baja, Szegedi út, Kt. 766, Hungary.
e-mail: borko@electra.bajaobs.hu
[12] Konkoly Observatory, Research Centre for Astronomy and Earth Sciences, H-1121 Budapest, Konkoly Thege Miklós út 15-17, Hungary
[13] ELTE Eötvös Loránd University, Gothard Astrophysical Observatory, Szent Imre h. u. 112, 9700 Szombathely, Hungary
[14] HUN–REN–ELTE Exoplanet Research Group, H-9700 Szombathely, Szent Imre h. u. 112, Hungary
[15] SETI Institute, 189 Bernardo Avenue, Suite 200, Mountain View, CA 94043, USA
[16] Astronomical Institute of the Wrocław University, ul. Kopernika 11, 51-622 Wrocław, Poland
[17] Copernicus Astronomical Center, Bartycka 18, 00-716 Warsaw, Poland

Received March 8, 2026

ABSTRACT

Aims. We are attempting to better understand how stellar pulsations in close binary systems are affected, and possibly induced, by tidal, Coriolis, and centrifugal forces.
Methods. We analyzed TESS data for some 50,000 potential eclipsing binaries selected by machine learning algorithms in order to search for pulsation multiplets split by integer multiples of the orbital frequency.
Results. We report on the discovery of an octupole pulsation mode in the binary star system TIC 287869463, which contains a δ Scuti star. This mode is actually a combination of Y_{3+3} and Y_{3-3} modes that are perturbed into a new eigenmode of the star via tidal, Coriolis, and centrifugal forces, which we call a 'Y_{33+}' mode. The mode is stationary on the star as opposed to being a traveling wave around the pulsation equator. To our knowledge, this is the first time that such an $\ell = 3$ mode identification has been made in any δ Scuti star, and the first stationary $\ell = 3$ sectoral mode of this type seen in any star, including the Sun. The $\ell = 3$ pulsations appear as a combination of two components at 34.94616 d^{-1} and 39.31132 d^{-1}, split by exactly six times the frequency of the orbital motion to within better than 1 part in 10^5. We extract the pulsation frequencies from the TESS data spanning more than three years, and model the system to gain a better understanding of this novel asteroseismic discovery. The pulsation frequencies are found to be steadily increasing with time, but always maintaining a split equal to six times the orbital frequency.
Conclusions. We discuss the implications for the broader class of "tidally tilted pulsators" and "tri-axial pulsators" that have been discovered to date. We conclude that these previous categories can all be interpreted as linear combinations of spherical harmonics whose axes coincide with the orbital axis and form new eigenmodes of the star via tidal, Coriolis, and centrifugal perturbations

Key words. (stars:) binaries (including multiple): close — (stars:) binaries: eclipsing — (stars:) binaries: general — stars: variables: delta Scuti

1. Introduction

Stellar pulsations have been studied for more than a century since 1919, when Eddington began an exploration of the theory of stellar pulsation with particular interest in understanding Cepheid variables (Eddington 1919a,b, 1926). For the first half-century of the study of stellar pulsation it was assumed that the surface geometry of pulsation modes could be described adequately by spherical harmonics (Cowling 1941), which are the eigenmode solutions to pulsation equations for perfectly spherical stars. The eigenmodes associated with the spherical harmonics have three quantum numbers describing their geometry: n, the radial overtone, which is the number of radial nodes that are spherical shells, ℓ, the degree, which is the number of surface nodes of the mode, and m, the azimuthal order, which gives the number of surface nodes that are lines of longitude. It was further assumed that the axis of pulsation coincided with the rota-

tion axis of all pulsating stars, since that, in most cases, is the principal axis of distortion from spherical symmetry (see, e.g., Kurtz 2022 and Aerts et al. 2010 for reviews).

Traditionally, in stars other than the Sun, the degree of the mode is inferred, rather than observed directly. Surface cancellation of observed sectors of the spherical harmonics has meant that modes of higher degree ($\ell \geq 3$) have not been detected at all, since these higher degree modes have very low visibility (Dziembowski 1977). On the other hand, because the Sun has a well-resolved surface, modes of very high degree can be detected to beyond $\ell = 300$ (Larson & Schou 2011, Scherrer et al. 2012, Larson & Schou 2015). Observation and knowledge of these high-degree modes place major constraints on the structure of the Sun via helioseismology.

Since we know that the Sun pulsates in very high degree modes, we can reasonably conjecture that other stars do, too. How do such high-degree modes affect the structure of a pulsating star, its evolution, its internal rotation and angular momentum transfer? The answers to these important questions can be illuminated by the direct observation of modes of degree $\ell \geq 3$.

Kurtz (1982) discovered the rapidly oscillating Ap (roAp) stars and demonstrated for the first time that some stars have pulsation axes that are inclined to the rotation axis of the star. In the case of the strongly magnetic roAp stars, that pulsation axis is close to the magnetic axis, which is itself inclined to the rotation axis. Kurtz (1982) proposed the oblique pulsator model to explain the pulsation amplitude and phase variations seen to occur in roAp stars with rotation. Simply, this shows that as an obliquely pulsating star rotates, the geometry of the degree of the pulsation mode becomes visible because the mode is seen from differing aspect. In effect, observers get to 'walk around' the star and see the non-radial modes from different aspect, thus exposing the number and positions of the surface nodes.

More recently, data from the Transiting Exoplanet Survey Satellite (TESS; Ricker et al. 2015) enabled the identification of two δ Scuti stars in binaries with pulsations largely confined to one hemisphere with respect to the tidal axes on the L1 side (Handler et al. 2020; Kurtz et al. 2020). These were dubbed "single-sided pulsators". HD 74423 had one prominent pulsation mode with a half-dozen components separated by the orbital frequency $\nu_{\rm orb}$ and a systematic change in pulse phase by π radians every orbit. CO Cam had four such modes, each with components also separated by $\nu_{\rm orb}$. In these systems, there were systematic phase changes when the pulsation amplitude was near zero in each of these modes.

These modes were discovered largely because of their visually striking "single-sidedness", but this complication also made it difficult to understand the nature of the underlying modes themselves from the Fourier transforms (FTs). At the time, it was assumed that the axes of these pulsations lie along the tidal axis, i.e., that they were "tidally tilted modes", wherein the pulsations were tidally trapped on one hemisphere and suppressed on the other (Fuller et al. 2020).

Rappaport et al. (2021) reported a much simpler multiplet mode in a δ Scuti pulsator in a binary system, with no single-sidedness. This mode had two prominent equal-amplitude components separated by 2 $\nu_{\rm orb}$ with two weak peaks on either side of the larger peaks and separated by 1 $\nu_{\rm orb}$. There were two maxima in this pulsation mode around the orbit (at the ellipsoidal light variation, 'ELV', maxima), and phase jumps of π rad at the eclipses. This was interpreted as a tidally tilted Y_{11x} mode, where the x refers to the pulsation axis lying along the tidal axis (the $\hat{x}$ direction)[1].

Building on these discoveries, Jayaraman et al. (2022) identified 31 pulsation modes a pulsating sdB star with a white dwarf companion. These modes typically had between 3 and 5 components separated by $\nu_{\rm orb}$, with one or two π phase jumps per orbit. These were not simple to understand, but were interpreted at the time as tidally tilted Y_{1mx} or Y_{2mx} modes.

More recently, TESS data revealed two δ Scuti stars in binary systems with rich pulsation spectra—9 and 14 doublets (Zhang et al. 2024; Jayaraman et al. 2024), which we interpreted as simple dipole pulsation modes. Each of these modes consists of just two dominant components separated by 2 $\nu_{\rm orb}$ with either no detectable central component, or a weak one. Each mode has two amplitude maxima per orbit, either at the eclipses, or at the ELV maxima. Each also has two π phase jumps per orbit, either at the ELV maxima, or at the eclipses, respectively. These were interpreted as Y_{10x} or Y_{10y} modes, depending on where the modes had their amplitude maxima.

Fuller et al. (2025) modeled these systems as an entirely new type of mode which consist of linear combinations of Y_{1+1z} and Y_{1-1z} modes that are coupled by tidal, centrifugal, and Coriolis forces in the binary. This modeling revealed that linear combinations of Y_{1+1z} and Y_{1-1z} modes produce, and are mathematically identical to, tidally tilted modes Y_{10x} and Y_{10y}. Thus, either interpretation is valid. However, as Fuller et al. (2025) also showed, other higher order modes with pulsation axes along z (i.e., with $\ell = 2$ and $\ell = 3$) can also be combined via tidal, centrifugal, and Coriolis forces to produce new eigenmodes of the star. These modes also have multiplet frequencies that are spaced by integer multiples of $\nu_{\rm orb}$ and can exhibit up to 4 and 6 amplitude maxima, respectively, per orbit as well as up to 4 and 6 π phase jumps.

These latter Fuller modes are all linear combinations of spherical harmonics with pulsation axes lying along the spin (or orbital) axis. To the lowest order, modes of the same ℓ and differing by $\Delta m = 2$ are coupled by the tidal forces (Fuller et al. 2025). We note that for $\ell \geq 2$ the degeneracy is broken, and these are no longer equal to, or even mimic, simple pulsation modes that have been tidally tilted along either the x or y axes. Thus, it is now possible within this paradigm to distinguish between tidally *coupled* "z" modes and tidally *tilted* modes whose pulsation axes lie along $\hat{x}$.

All of the 'tidally tilted' and 'tri-axial' modes mentioned above can be reinterpreted as Fuller modes, mostly with $\ell = 1$ and $\ell = 2$ components that may be substantially suppressed in one of the tidal hemispheres. Here, we report the discovery of a δ Scuti pulsator in a binary system (TIC 287869463) which exhibits a Fuller octupole pulsation mode that cannot be described as any kind of tidally tilted pulsation. While $\ell = 3$ pulsation modes have been found in red giants (Stello et al. 2016) and in some main sequence solar-like oscillators (e.g., Kjeldsen et al. 2005), no such modes have been reported in δ Scuti stars or in other opacity-driven pulsating stars. Moreover, no previously-discovered $\ell = 3$ sectoral mode is stationary, i.e., non-circulating.

In Sect. 2 we present observational evidence for these modes and show how the amplitudes of these modes vary with time, while the phase differences between the upper and lower frequency components remain constant to within the statistical un-

[1] We take the $\hat{z}$ and $\hat{y}$ directions to lie along the angular momentum vector of the binary and the direction in the orbital plane perpendicular to the tidal axis, respectively.

Table 1: Sectors and Cadence for TIC 287869463

S87, S90, S93	200-s
S63, S64, S65, S66	200-s
S30, S33, S36, S37, S39	600-s
S3, S6, S10, S11, S12, S13	30-min

Table 2: Properties of TIC 287869463[a]

RA [degree]	127.9633
Dec [degree]	−75.4937
G	11.87
B_p	12.01
R_p	11.63
$B_p - R_p$	0.379
pmra [mas yr^{-1}]	1.89
pmdec [mas yr^{-1}]	−2.42
radial velocity [km s^{-1}]	27.58
RV_amp_robust[b] [km s^{-1}]	144
distance [pc]	1086 ± 3
$P_{\rm orb}$ [d][b]	1.374 536

Notes. (a) From Gaia DR3 unless otherwise noted. (b) From this work. (b) This parameter, taken from Gaia, represents approximately twice the K_1 amplitude (Katz 2023).

certainties. Simulations of these and other Fuller modes are presented in Sect. 3, wherein we highlight the striking similarity between the simulated frequency peaks and what we observe in TESS data. An analysis of the binary system parameters is undertaken in Sect. 4. We summarize and discuss our results in Sec. 5. In the Appendix, we discuss O-C diagrams for the pulsations and show that the pulsation frequencies are steadily increasing over the 5-yr interval of the TESS observations.

2. Discovery of Fuller Modes in TIC 287869463

We are currently carrying out an extensive search for Fuller-mode pulsators in TESS data. In particular, we are examining a set of bright likely eclipsing binaries (TESS magnitude $T_{\rm mag} <$ 13.5) selected by machine learning from 56 sectors of TESS observations with 10-minute cadence or shorter (Kostov et al. 2025; Powell 2026; Jayaraman et al., in prep). In all, there are 51,820 such candidate binaries whose $T_{\rm eff}$ falls in the range for them to contain possible δ Scuti pulsators (6500 K $\leq T_{\rm eff} \leq$ 9000 K). The TESS light curves used for the search are taken from the MIT Quick-Look Pipeline (QLP; Kunimoto et al. 2021, 2022).

For each candidate binary, we produce an automated echelle diagram, which plots the pulsation frequency against the "echelle phase" (the pulsation frequency $\nu_{\rm puls}$ modulo $\nu_{\rm orb}$, normalized to $\nu_{\rm orb}$). To do so, we first determined the orbital period $P_{\rm orb}$, if any, and then subtracted the first 30 harmonics of $\nu_{\rm orb}$ from the light curve. We then sequentially identified and removed from the remaining light curve the 75 highest-amplitude pulsation frequencies in the FT, or the highest-amplitude pulsations down to a noise floor of 5 times the rms amplitude in the FT—whichever came first. The echelle diagrams were created from these highest-amplitude peaks. Finally, we examined each echelle diagram by eye for interesting modes that are split by integer multiples of the orbital frequency. Most of the split modes are dipoles (split by $2\nu_{\rm orb}$), along with a smaller percentage of quadrupoles (split by 4 $\nu_{\rm orb}$). However, we identified one target (TIC 287869463 or Gaia DR3 5216608316411701248; Stassun et al. 2019) as having an octupole mode, split by 6 $\nu_{\rm orb}$.

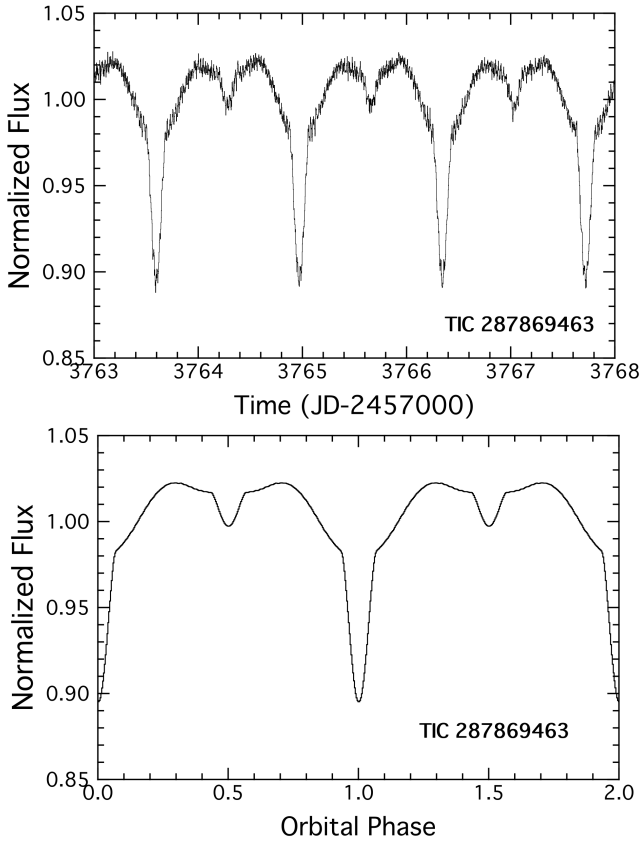

Fig. 1: Light curves for TIC 287869463. *Top*: 5-d segment of the raw TESS light curve. The pulsations superposed on the eclipsing light curve are readily apparent. *Bottom*: Fourier-reconstructed light curve from the first 60 orbital harmonics. Here, we used only the cosine terms in the reconstruction to remove a small, time-varying, O'Connell effect (O'Connell, 1951), presumably arising from star spots on the cooler companion star.

A short 5-d segment of the TESS light curve for TIC 287869463 is shown in Figure 1 (top panel). The stellar pulsations of the hotter component can be seen superposed on the eclipsing light curve. In all, there are 7 sectors of data with a 200-s cadence, for a total of about 168 d of data, with 100 d of that being contiguous. A Fourier-reconstructed light curve made from the first 60 orbital harmonics is given in Figure 1 (bottom panel). Table 1 lists all TESS sectors in which TIC 287869463 was observed, alongside the observing cadence. Table 2 enumerates photometric and astrometric information about TIC 287869463, and the system properties (modeled in Section 4).

The Fourier transform of the 200-s cadence data from Sectors 63-66 (100 d of nearly continuous data) is shown in Fig. 2. The data were cleaned of the first 40 orbital harmonics before computing the FT. The FT shows 6 prominent peaks due to stellar pulsations, all in the frequency range ~35-40 d^{-1}. The dipole pulsation modes (separated by $2\nu_{\rm orb}$) are labeled "D1" and "D2" , and the octupole mode—separated by $6\nu_{\rm orb}$—is labeled as "O1."

The echelle diagram for this star's pulsations is shown in Figure 3. The D1 mode has a small central component, while D2 does not. The octupole mode is split by 6 $\nu_{\rm orb}$, and has only one tiny intermediate frequency peak, which is situated at 1 $\nu_{\rm orb}$ from the missing central frequency. There are also two low amplitude singlet modes at 35.976 and 41.096 d^{-1}.

Table 3: Frequencies of the 6 prominent pulsations seen in TIC 287869463[a]

Frequency d^{-1}	Amplitude mmag	Phase Difference[b] degrees	Mode ID ...	Frequency Split d^{-1}	Inferred P_{orb}[c] d
38.45620(1)	1.0 – 2.5	+2.3 ± 1.1	Dipole 1a	...	...
39.91123(1)	1.2 – 2.6	+2.3 ± 1.1	Dipole 1b	2 × 0.727516(20)	1.374539
36.36627(2)	0.5 – 2.4	181.2 ± 0.9	Dipole 2a	...	...
37.82130(2)	0.6 – 2.7	181.2 ± 0.9	Dipole 2b	2 × 0.727514(34)	1.374544
34.94617(3)	0.2 – 0.6	180.4 ± 3.7	Octupole 1a	...	...
39.31127(3)	0.3 – 0.7	180.4 ± 3.7	Octupole 1b	6 × 0.727518(39)	1.374537

Notes. (a) All frequencies are referenced to an epoch of BJD 2460000. Values in parentheses are the uncertainties in the last digits. See Table A.1 for details of how the frequencies are changing with time. (b) Average phase differences between the two mode components. See Fig. 4 for a graphical representation. Phases are taken at the time of primary eclipse. (c) The orbital period at the common epoch is 1.374,536,0(2) d.

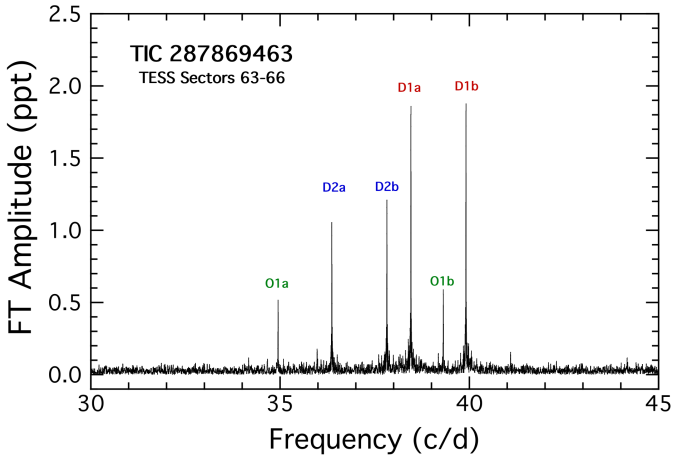

Fig. 2: Fourier transform of the TESS data from Sectors 63 to 66 for TIC 28786963. The labels mark the two dipole modes ('D1' and 'D2') and an octupole mode ('O1'). Each mode has two prominent components, marked 'a' and 'b'. The dipole components are separated by 2 ν_{orb}, while the octupole components are separated by 6 ν_{orb}.

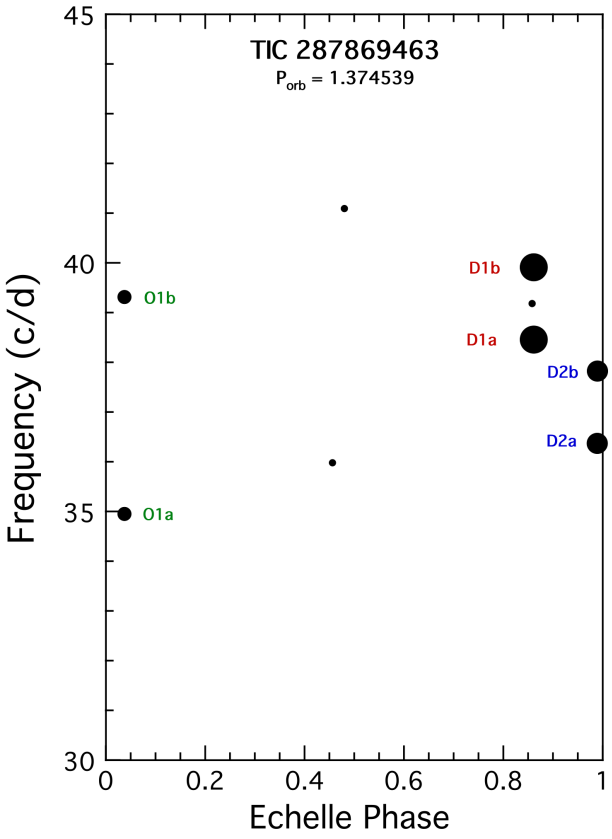

Fig. 3: Echelle diagram for TIC 287869463 constructed from the TESS data of Sectors 63-66. This shows the frequencies of the pulsations vs echelle phase—the frequency modulo ν_{orb} and normalized to ν_{orb}. The labeling of the components follows Fig. 2.

The six most significant frequencies seen in the periodogram and echelle diagram, related to D1, D2, and O1, are enumerated in Table 3. These frequencies were produced from phase tracking of the pulsations (see, e.g., Bowman et al. 2016, and also Appendix A) over all 12 sectors of 200-s and 600-s cadence data (where the pulsation frequencies were below the Nyquist frequency). All frequencies are referenced to a common epoch, BJD = 2460000. In the 5th column of Table 3, we list the mean frequency split between the two components of the particular mode. In the last column, we indicate the (orbital) period inferred from the splitting, and these values all agree to within 10^{-5} d of the calculated orbital period[2].

The amplitudes and phases of the 6 pulsations as a function of TESS sector are given in the top and bottom panels of Fig. 4, respectively. The amplitudes of the two components of each of the dipoles are clearly correlated, as are the two amplitudes of the octupole mode. However, the latter are less variable than for the D1 and D2 modes. The two amplitudes for each pulsation mode are always very similar and are not varying independently.

In the phase plot (Fig. 4, bottom panel), we show the phase difference between the two components of each mode as a function of TESS sector, all referenced to a time of primary eclipse (BJD = 2460014.4757). For the D1 mode, the two components are mostly always in phase at the primary eclipse. The two components of both the D2 and O1 modes are essentially always out of phase by 180° at the primary eclipses. (This in turn means that these modes are at an amplitude minimum at primary eclipse.) The standard errors in the phase differences are 1.1°, 0.9°, and 3.7°, for the D1, D2, and O1 modes, respectively.

We next force fit a three-element triplet in frequency (separated by ν_{orb}) to each of the dipole modes, and a 7-element septuplet to the octupole mode. We use the amplitudes and phases of the extracted mode elements to reconstruct the amplitudes of the three pulsation modes as a function of orbital phase. These results are shown in the top panel of Fig. 5. An amplitude-scaled orbital light curve is shown superposed for phasing reference.

[2] The apparent orbital period is also changing with time, and the cited orbital period is also referenced to this same epoch of BJD = 2460000 (see Appendix A).

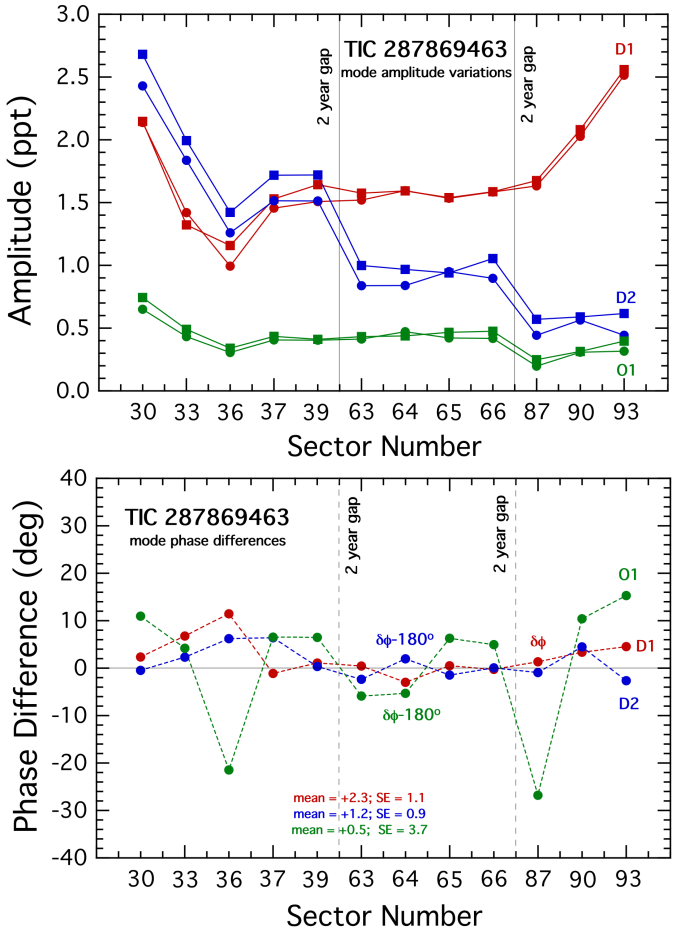

Fig. 4: *Top*: Variations in the dipole (red and blue) and octupole (green) component amplitudes with sector number across ~5 yr. Note that for each mode, the two component peaks have very similar amplitudes, and their variations are clearly tightly correlated. *Bottom*: The difference in phase between the two components of each of the three modes, at the times of primary eclipse. To fit all three curves on the same scale, we subtracted 180 degrees from the phase difference of modes D2 and O1. This shows that the phase differences remain constant at either 0 or π rad to within the few degrees of our statistical precision. This analysis shows that the geometry of the modes remains unchanged over the time span of the observations.

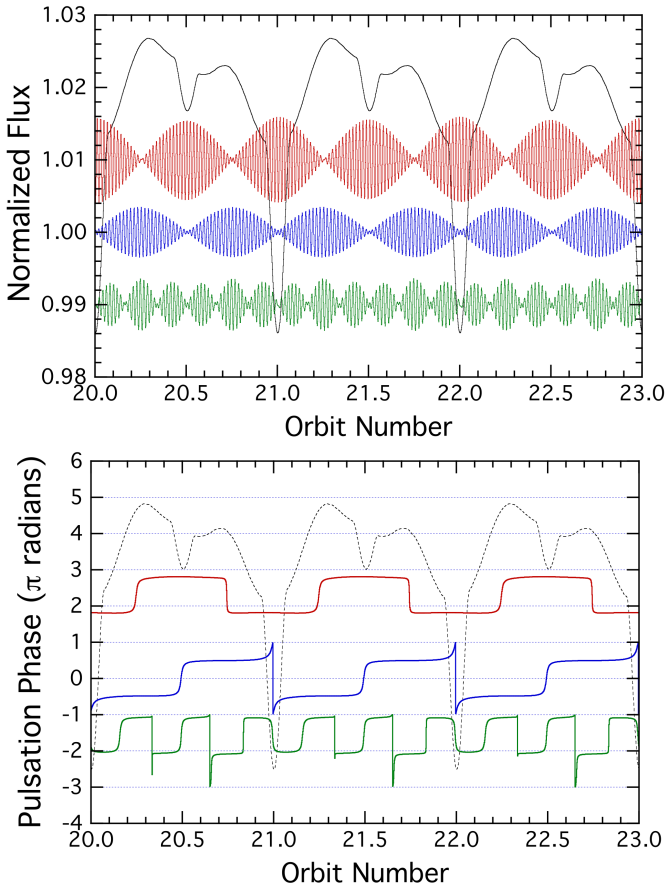

Fig. 5: Reconstructions of pulsation amplitude and phase vs the orbital phase. The color coding, top to bottom, is red = D1, blue = D2, and green = O1. Superposed is a scaled version of the orbital light curve to guide the eye on the orbital phasing. Note the 6 maxima in pulsation amplitude and six π-rad phase jumps per orbit for the octupole (O1).

Each of the dipoles has two amplitude maxima per orbit, while the octupole has six such maxima. We find that D1 has a maximum amplitude at the eclipses, while D2 has a minimum there. The octupole mode also has a pulsation minimum at the eclipses. These are all in accord with the discussion above of the phase differences of the two elements of each mode (see also Fig. 4) at the time of primary eclipse. The bottom panel of Fig. 5 shows the run of reconstructed pulse phase vs orbital phase. The dipole modes have two π phase jumps each orbit, while the octupole mode has six π phase jumps.

There are several arguments that point to the octupole mode in this star—the first such stationary $\ell = 3$ sectoral mode discovered—being a single pulsation mode split by 6 $\nu_{\rm orb}$, as opposed to two independent modes that are coincidentally separated by ~6 $\nu_{\rm orb}$. First, the separation of the octupole mode elements corresponds to an integer multiple of the measured orbital period to one part in 10^5. The odds of this occurring at random for the two significant non-dipole frequencies over the pulsation range of 30-40 d^{-1} is only 1.7×10^{-6} (verified by Monte Carlo simulations). Second, the very similar amplitudes of the two mode components, and their correlated amplitude and frequency variations over a 5-year interval (see Appendix A), also strongly suggest that these are not from independent modes. Third, the fact that this mode has either a minimum or maximum at the time of primary eclipse (minimum in this case) would only occur at random about 30% of the time.[3] We also note that there is a well-developed model (Fuller et al. 2025) that predicts such modes, and this adds confidence to the interpretation of this as an octupole mode.

3. Simulations of the modes and Interpretation

Our analysis of the TESS data for this star has shown that we have found an octupole mode of the form:

$$Y_{33+} = (Y_{3+3z} + Y_{3-3z})\, e^{i\omega t} = \left(y^3 - 3x^2 y\right) \sin(\omega t), \quad (1)$$

[3] This results from the fact that in such an octupole mode, there will be either a minimum or maximum every 30°, and we have an accurate determination of the mode phase to within ±4.7°

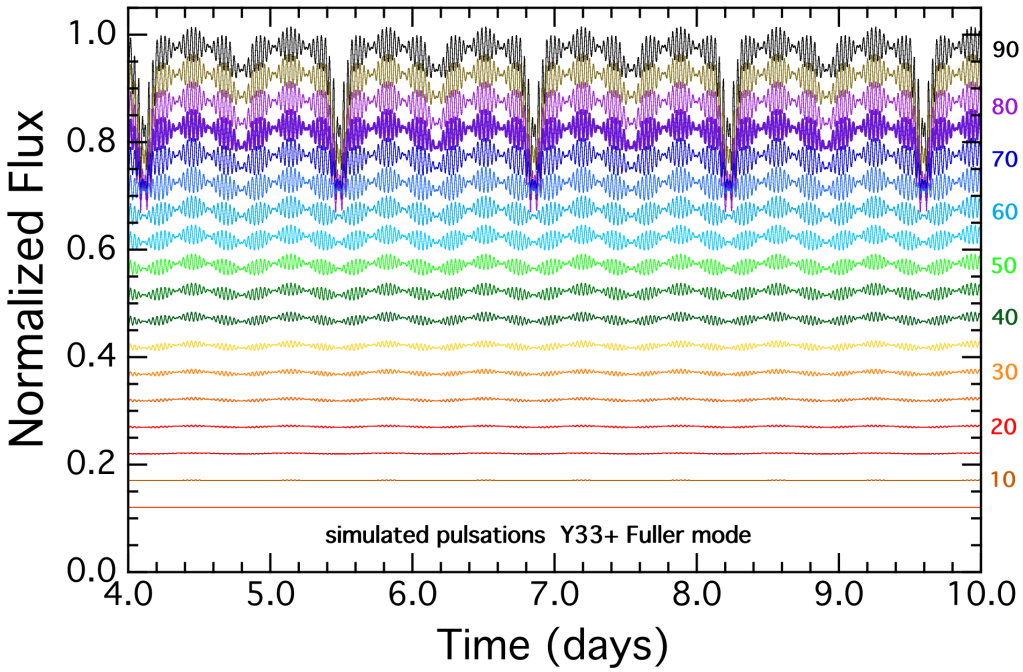

Fig. 6: Simulated light curves of TIC 287869463 with a Y_{33+} pulsation mode. The orbital inclination angles in degrees are written next to the right-hand y axis. The purple curve for $i = 75°$ is highlighted since that is the approximate inclination angle for TIC 287869463.

where the Y's on the right hand side of the top equation are ordinary spherical harmonics with $\ell = 3$ and $m = \pm 3$. The extra 'z' designation indicates that the axis of these modes lies along the rotation vector of the pulsating star, which in turn we assume is aligned with the orbital angular momentum vector (along $\hat{z}$). These spherical harmonics have a traveling wave propagating around the star's equator. Fuller et al. (2025) showed how such modes can be coupled by perturbations on the pulsating star in a binary from tidal, Coriolis, and centrifugal forces into a stationary mode (standing wave) in the rotating star's reference frame.

The Y_{33+} mode is a standing wave sectoral octupole mode in a frame rotating with the orbital motion. Here, the + sign indicates the sum, rather than the difference, between the terms on the right side of Equation 1. This mode differs from standard sectoral Y_{3+3z} or Y_{3-3z} modes due to its stationary nature. Throughout the orbital cycle, we can therefore observe this mode from varying angles. This gives the same advantage of providing information on the geometry of the mode (and its viewing aspect), as is gained from oblique pulsation in roAp stars. Such geometric information cannot be extracted from rotationally perturbed normal sectoral octupole modes pulsating about the rotation axis.

Previously, we identified numerous stationary dipole modes formed from $Y_{11\pm}$ modes ($Y_{1+1z} \pm Y_{1-1z}$) (Zhang et al. 2024; Jayaraman et al. 2024). We are also working on a smaller set of other pulsators with related quadrupole modes formed as $Y_{22\pm} = Y_{2+2z} \pm Y_{2-2z}$ (see, e.g., Handler et al. 2025). As described in Fuller et al. (2025), there are three other perturbed stationary $\ell = 2$ modes, and five other $\ell = 3$ modes in addition to the two described above. However, these other $\ell = 3$ Fuller modes have components split by either 2 or 4 times the orbital frequency and can be difficult to distinguish from $Y_{11\pm}$ or $Y_{22\pm}$ modes.

In order to make concrete some of the properties of the new stationary perturbed modes, we have developed a code to simulate such pulsations in a binary star system. We utilize two stationary spherical stars separated by the semi-major axis of the binary a. We uniformly distribute 7000 unit vectors on each star, and then view the system from the perspective of an observer orbiting around the binary at frequency $\nu_{\rm orb}$, at an inclination angle i. Any pulsation mode can then be assigned to the fixed pulsating star; this mode can be either circulating or stationary[4]. The pulsation amplitudes are arbitrary since we have no way of calculating these a priori. At a given time, we evaluate the dot product between the viewing direction's unit vector and the unit vectors over the surface of both stars. If the dot product is negative, then the observer sees that part of the star; all the visible flux (as calculated in this manner) is then summed. Eclipsed regions are also excluded from the sum. This same dot product is also used to compute the limb darkening and the projected area of the surface element. We also add a simple cosine term of $2\nu_{\rm orb}$ to represent an ellipsoidal light variation for aesthetic purposes.

This set of calculations is done every 120 s (to match the TESS 2-min cadence) for 50,000 steps (to roughly match three sectors of TESS data). The simulated time series is cleaned of orbital harmonics, as is done for the real data set. We then take the Fourier transform of the simulated data. The entire process is then repeated for 18 orbital inclination angles between 90° and 5°. An illustrative set of simulated light curves for a Y_{33+} mode is shown in Fig. 6. Each light curve has six pulsational maxima per orbit with minima (in this particular case) at both eclipses. In general, the relative pulsation amplitude decreases with decreasing inclination angle, going to zero at $i = 0$, as expected. We highlight the curve at $i = 75°$ because that is close to the inclination determined for TIC 287869463 (see Sect. 4).

Fourier transforms of simulated data for four different $\ell = 3$ modes are shown in Fig. 7. In the upper left panel, we display the FTs for a Y_{33+} mode of the type detected for TIC 287869463 as a function of orbital inclination angle. There are two main

[4] We assume that the fractional flux, $\delta F/F$, emerging from each surface element of the star due to the pulsation is simply proportional to the $Y_{\ell,\rm m}$ of the particular mode being simulated.

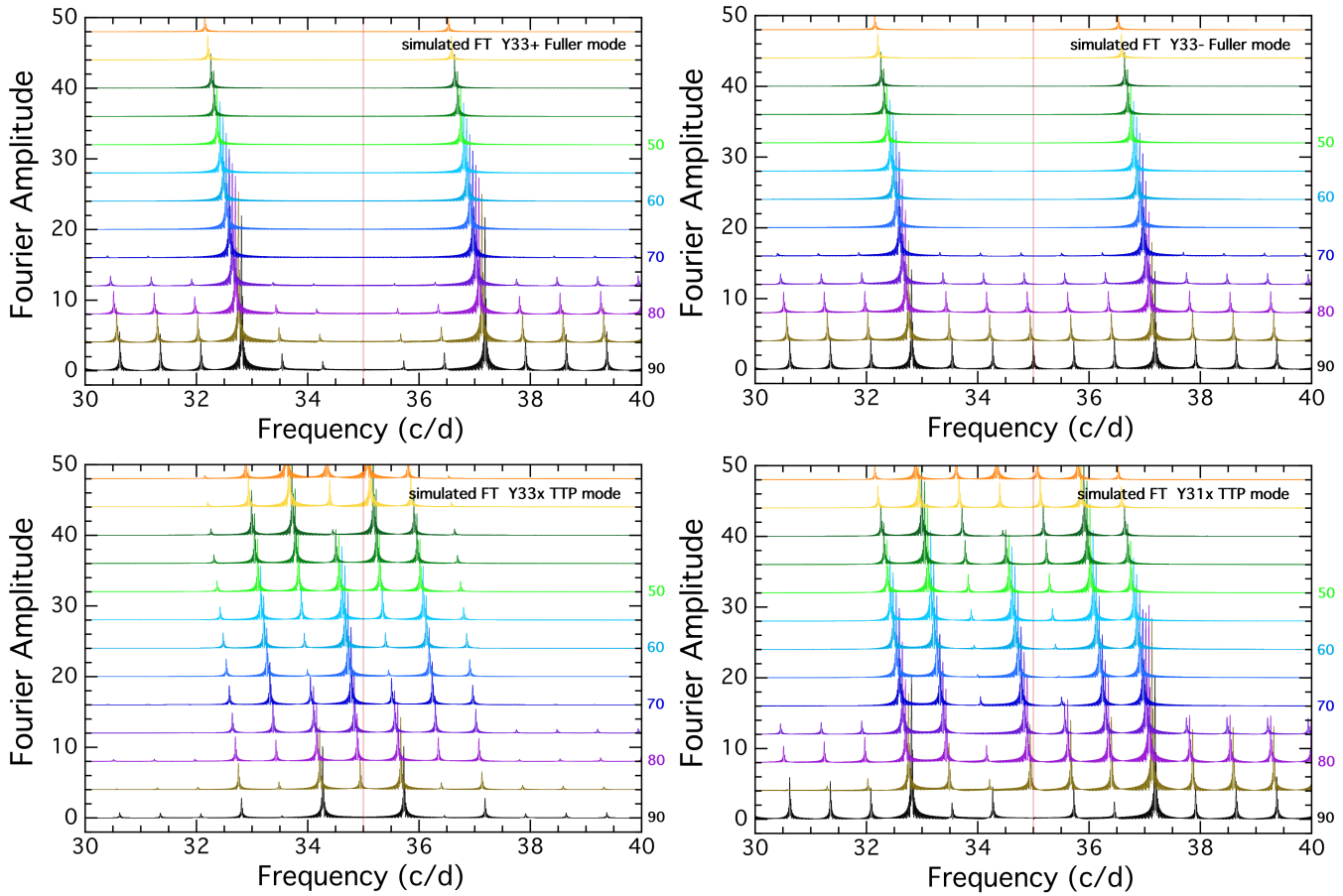

Fig. 7: Simulated Fourier transforms for different examples of $\ell = 3$ pulsation modes. The modes represented in the four panels are Y_{33+}, Y_{33-}, Y_{33x}, and Y_{31x}, clockwise starting from the upper left panel. The first two modes are defined in Sect. 3 and equation (1). The latter two modes have had their pulsation axis tilted into the orbital plane, and lying along the tidal (or 'x') axis. The FT peaks are arbitrarily shifted to the right for decreasing inclination angles to avoid overlapping peaks.

peaks that are separated by 6 $\nu_{\rm orb}$. The smaller peaks for $i \gtrsim 80°$ are due to the eclipses periodically modulating the intensity of the pulsations, a phenomenon known as "spatial filtration" (Gamarova et al. 2003; Reed et al. 2005; Biró & Nuspl 2011; Johnston et al. 2023; Van Reeth et al. 2023). For an inclination of ∼75° (as observed for TIC 287869463), these frequency peaks would not have been detected. In the upper right panel, we show the corresponding FTs for a Y_{33-} mode, and the results are similar to those for a Y_{33+} mode. The main difference is that the small intermediate peaks are somewhat more pronounced. This is due to the fact that the pulsation amplitudes are a maximum at the eclipses, rather than a minimum, and this enhances the effects of the eclipses on the pulsation's visibility. But, even at $i \simeq 75°$, these smaller peaks would have been only barely detectable.

A pictorial representation of the Y_{33+} mode and the Y_{33-} mode, as they might appear in the context of TIC 287869463, is shown in Figure 8.

In the lower two panels of Fig 7 we show the FTs for simulated data of two different $\ell = 3$ modes, namely a Y_{33x} and Y_{31x} mode. Here, the "x" signifies that the pulsation axis is tilted into the orbital plane and lies along the tidal axis. As mentioned above, these are "tidally tilted" pulsations, and they have traveling waves propagating around the x axis. As shown by the simulations, there are numerous intermediate peaks out to $\pm 3\,\nu_{\rm orb}$. We remind the reader that the central peak of each multiplet is the only pulsation mode frequency; all of the other components of the multiplet are Fourier descriptions of the observed pulsation amplitude and phase modulating with changing orbital aspect. These multiplets in the lower two panels look nothing like what we see in TIC 287869463. We have simulated all combinations of traveling and stationary modes around all three axes, x, y, and z with $\ell = 3$, and the only mode that fits the observational data (FT and the phasing of amplitudes and pulse phases with respect to the eclipses) for TIC 287869463 is a Y_{33+} octupole Fuller mode.

4. Analysis of the Binary System

To evaluate the properties of the two stars in TIC 287869463, we simultaneously fit the spectral energy distribution (SED) curve and the TESS light curve. We employ a Markov Chain Monte Carlo (MCMC) algorithm to fit for the stellar masses M_1 and M_2 (where M_1 is the more massive, pulsating star), the system age, the orbital inclination angle i, interstellar extinction, A_V, and the distance. The latter two parameters could be fixed at the values from Gaia. In total, there are between 4 and 6 free parameters. We assume that the binary has evolved in a coeval fashion—there has been no prior mass transfer or mass loss from the system. We thus can use stellar evolution models (Choi et al. 2016; Dotter 2016) to determine the radii and $T_{\rm eff}$ of both stars, which are uniquely determined given their masses and age.

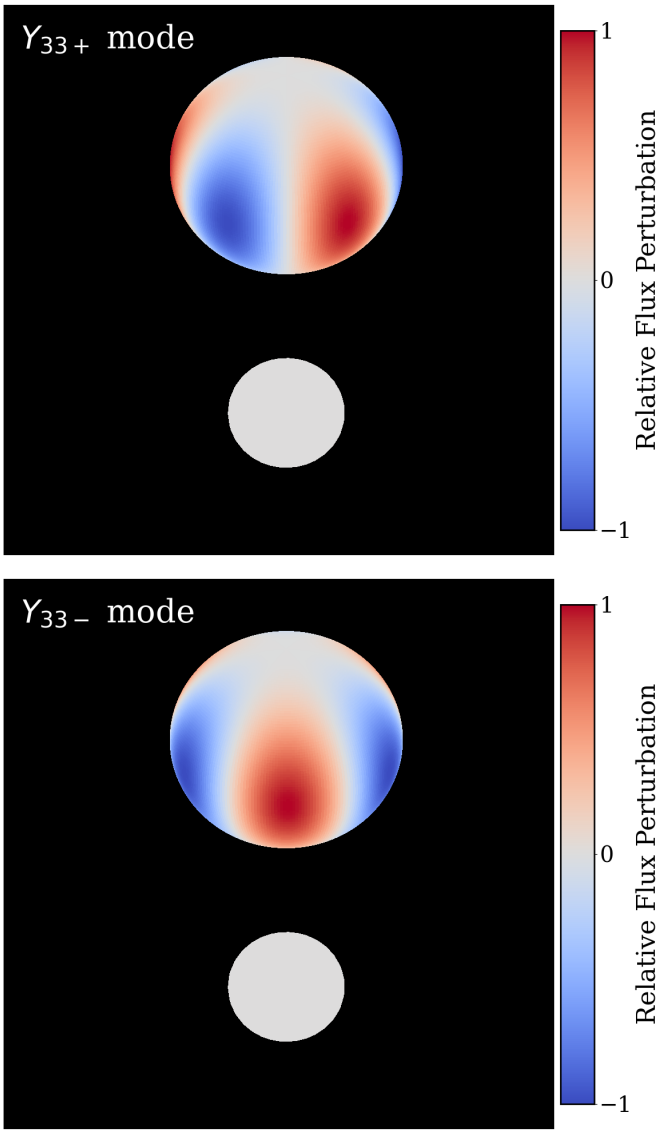

Fig. 8: Diagrams showing the flux perturbation across the surface of a star pulsating in the Y_{33+} mode (top) and Y_{33-} mode (bottom). The diagram corresponds to orbital phase zero for an observer viewing at at inclination $i = 55°$ relative to the orbital axis. The observed phase of the amplitude modulation of the O1 mode is consistent with that of a Y_{33+} mode.

The input information we use includes: (i) 23 available SED points spanning 0.15 μm to 11.6 μm, (ii) an approximate value for K_1 of the radial velocity (RV) curve[5], (iii) the eclipsing light curve profile, (iv) the Gaia distance of 1086 ± 3 pc (Bailer-Jones et al. 2021), and a Gaia value for A_G of 0.709[6]. Additionally, we use the MIST evolution tracks (Paxton et al. 2011, 2015; Choi et al. 2016; Dotter 2016; Paxton et al. 2019) to relate the stellar mass and age to its radius and $T_{\rm eff}$. In order to compute the model stellar spectra from the radii and $T_{\rm eff}$ of the stars, we make use of the Castelli & Kurucz model stellar atmospheres (Castelli & Kurucz 2003), assuming a solar metallicity. Finally, we correct for interstellar extinction using the prescription presented in Cardelli et al. (1989).

We collected the available archival spectral flux measurements (SED points) from 0.15 to 11.6 μm. These data were accessed from VizieR[7] (Ochsenbein et al. 2000) which, in turn, utilizes systematic sky coverage of such surveys such as Pan-STARRS (Chambers et al. 2016), SDSS (Gunn et al. 1998), 2MASS (Skrutskie et al. 2006), WISE (Cutri et al. 2013), and GALEX (Bianchi et al. 2017). More details about this type of SED fitting for binary star systems are given in Jayaraman et al. (2024); Handler et al. (2025); Yakut et al. (2025a,b).

When fitting a composite SED of two or more stars, it is important to have additional constraints between the properties of one star and the other(s). In particular, the eclipsing light curve in this system provides important information about such things as $T_{\rm eff,2}/T_{\rm eff,1}$, R_2/R_1, R_1/a, and the orbital inclination angle, where a is the semi-major axis of the system. Since well-developed light curve emulators such as Phoebe (Prša & Zwitter 2005) are not designed to work jointly with SED fitting codes, we have incorporated our own simple light curve emulator to help the SED fitter more properly separate the light contribution from the two stars (Jayaraman et al. 2024). This light curve emulator utilizes two spherical stars with limb darkening to generate eclipses. The out-of-eclipse behavior is described by three sinusoids of the form $\cos(\omega_{\rm orb}t)$, $\cos(2\omega_{\rm orb}t)$, and $\sin(\omega_{\rm orb}t)$ to represent such effects as ellipsoidal light variations, illumination effects, Doppler boosting, and corotating spots on the cooler star (see, e.g., Kopal 1959; Carter et al. 2011).

The best-fitting SED and light curve models are shown in the top and bottom panels of Fig. 9, respectively. The best-fitting system parameters derived from these fits are summarized in Table 4. The primary star, with a mass of 2.2 $M_\odot$, radius 2.6 $R_\odot$, and $T_{\rm eff,1}$ = 8734 K, has a luminosity typical of a δ Scuti star, with $T_{\rm eff}$ near the blue border of the δ Sct instability strip. The pulsator's parameters place it between the Balona et al. (2015) δ-Scuti-category boxes 4 and 7 in their Fig. 2. Pulsators in these categories can have pulsations up to ~50 d^{-1}, and there are many such systems with pulsations in a range similar to that which we see in TIC 287869463.

Finally, we point out that even though the secondary star contributes less than 1% of the system luminosity, we can be confident of having measured its parameters. The reason is that there are numerous constraints between the secondary and the primary other than from the SED, e.g., K_1, R_2/R_1, and T_2/T_1. Therefore, the primary star largely accounts for matching the SED, while the properties of the secondary star (including its contribution to the SED) come from the relative relations listed above, and a common age.

5. Discussion

While carrying out a large scale search for Fuller-mode pulsators in TESS data, we discovered an unprecedented octupole mode in a δ Scuti star. It is characterized by two peaks in the Fourier transform separated by $6\,\nu_{\rm orb}$. This splitting corresponds to 6 times the orbital frequency to within an accuracy of one part in 10^5. We argue that this cannot be just two random and unrelated modes of the pulsating star, but must comprise a single mode.

This octupole mode is actually a combination of ordinary Y_{3+3} and Y_{3-3} modes that are aligned with the stellar rotation axis. These are combined into a new eigenmode of the star by binary perturbations, and we call it a Fuller Y_{33+} mode

[5] We utilize the Gaia parameter RV_amp_robust of 144 km s^{-1} as a proxy for twice the RV amplitude K_1 (e.g., Katz 2023).

[6] This translates to an A_V of ~0.84 using either the rule-of-thumb factor of 1.2 or the detailed expression of Danielski et al. (2018); in particular their equation (3) and coefficients from row 5 of their Table 2.

[7] http://vizier.cds.unistra.fr/vizier/sed/

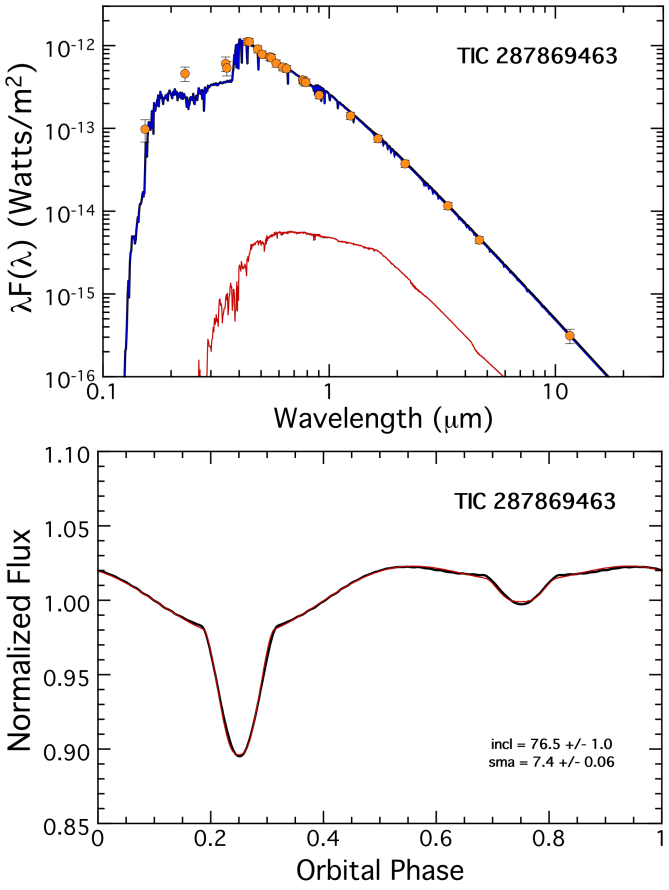

Fig. 9: *Top panel*: SED fit for TIC 287869463. The blue curve is the model spectrum for the primary star (the pulsator), and the red curve represents the model spectrum for the cooler, smaller secondary star. The black curve, nearly coinciding with the red curve, is the sum of the model fluxes. The orange points are measured SED points from the literature. For the SED fitting techniques and the origin of the data points, see Sect. 4. *Bottom panel*: Light curve fit using our custom light curve emulator. The black curve is the Fourier reconstructed light curve (i.e., the 'data') and the red curve is the model fit. See text for details.

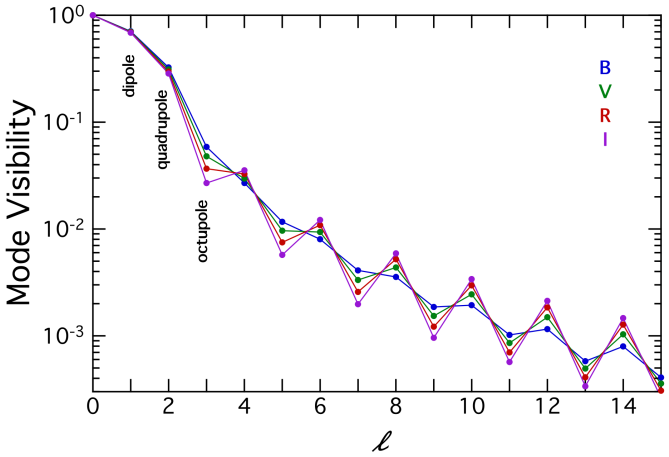

Fig. 10: Mode visibility diagram as a function of ℓ. These have been calculated as in Daszyńska-Daszkiewicz et al. (2002), for *BVRI* passbands; the red passband most closely matches that of TESS.

Table 4: Binary System Parameters[a]

Parameter	Value
M_1 [$M_\odot$]	2.18 ± 0.05
M_2 [$M_\odot$]	0.80 ± 0.03
R_1 [$R_\odot$]	2.57 ± 0.07
R_2 [$R_\odot$]	0.73 ± 0.03
$T_{\rm eff,1}$ [K]	8734 ± 200
$T_{\rm eff,2}$ [K]	4943 ± 150
L_1 [$L_\odot$]	34.7 ± 3.7
L_2 [$L_\odot$]	0.29 ± 0.04
a [$R_\odot$]	7.5 ± 0.3
Orbital Inclination [°]	76.5 ± 1.0
$P_{\rm orb}$ [d][b]	1.374 530
Primary Eclipse [BJD][b]	2460014.476
K_1 [km s^{-1}][c]	~72
A_V	0.80 ± 0.07
A_G[d]	0.709
Distance [pc][e]	1086 ± 3
age [Myr]	630 ± 50

Notes. (a) Based on the SED and light curve fitting, as described in Sect. 4, unless otherwise noted. (b) This work. (c) Half the value of the Gaia parameter RV_amp_robust. (d) Gaia's extinction. (e) Gaia's distance.

(Fuller et al. 2025). We presented a number of compelling reasons why the octupole mode cannot plausibly be two independent modes whose frequencies have an accidental alignment in the echelle diagram. This is the first octupole mode identified in any star with opacity-driven pulsations, and the first Fuller-type $\ell = 3$ stationary sectoral mode found in any star, including the Sun.

As we show in the Appendix, the pulsation frequencies of both the dipole and octupole modes are found to be steadily increasing with time, all at different rates. However, the splits in the mode frequencies remain constant at an integer multiple of the orbital frequency.

Because of geometric cancellation of higher-order ℓ modes over the visible hemisphere of pulsating stars, there is sharp decrease in the "visibility" of a pulsation mode with increasing ℓ. To investigate the visibility of higher degree modes we follow the approach described in Daszyńska-Daszkiewicz et al. (2002). As a first step, we approximate the mode visibility by the disc-averaging factor

$$b_\ell = \int_0^1 h(\mu) P_\ell(\mu) \mu d\mu \qquad (2)$$

where μ is the cosine of the viewing incidence angle and h is the limb darkening function. This should be reasonably accurate if the effects of rapid rotation and tidal interaction are neglected. In a more general approach, as in the case of the star we studied, the mode visibility may also depend on the azimuthal order m.

We show in Fig. 10 a plot of the visibility of pulsation modes in a star like TIC 287869463 as a function of ℓ for four different filters, including a red filter which is a reasonable approximation to the TESS bandpass (the results are also given numerically in Table 5). Dipole and quadrupole modes ($\ell = 1$ and $\ell = 2$, respectively) have relatively high visibilities of 0.7 and 0.3, respectively. However, for octupole modes ($\ell = 3$) the visibility drops abruptly to 0.037 (for the red filter). In TIC 287869463,

the dipole modes have amplitudes of 1.8 mmag and 0.8 mmag. However, the amplitude of the octupole mode is not too far below those, at 0.4 mmag. If we renormalize this according to the relative visibilities, we find that the octupole mode has an intrinsic amplitude of ∼10 mmag. Pulsation amplitudes of this size are fairly common among δ Scuti stars.

This exercise also shows that even hexadecapole modes with $\ell = 4$ should be as straightforward to detect as the octupole mode found here. However, higher modes with $\ell \geq 5$ will be very difficult to detect.

It is also worth noting that according to the simulations of Daszyńska-Daszkiewicz et al. (2006), the octupole mode should be relatively easy to identify from radial-velocity variations. Therefore, time-series spectroscopy could be used to validate our octupole mode identification for TIC 287869463.

Finally, we show in Figure 11 the location of the TIC 287869463 pulsator in the HR diagram. We plot five evolution tracks in the $T_{\rm eff}$ and R plane ...Jagoda: please write a short paragraph here on what you'd like to say about this plot and why this star will be so instructive to model for the two dipole and one octupole modes.

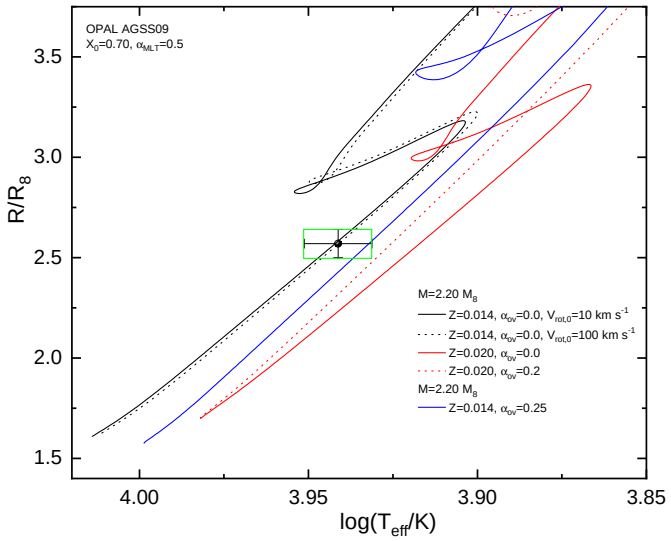

Fig. 11: Evolution tracks. Could you also draft up a short figure caption?

Acknowledgements. RJ is currently supported by a Klarman Fellowship from the College of Arts & Sciences at Cornell University. This project has received partial funding from the HUN-REN Hungarian Research Network. T.B. acknowledges the financial support of the Hungarian National Research, Development and Innovation Office – NKFIH Grant OTKA K-147131. VBK is grateful for financial support from NASA grant 80NSSC22K0747. GH thanks the Polish National Center for Science (NCN) for support through grant 2021/43/B/ST9/02972. JDD thanks the Polish National Center for Science (NCN) for support through grant 2023/50/A/ST9/00144. This paper includes data collected by the TESS mission. Funding for the TESS mission is provided by the NASA Science Mission Directorate. The QLP data used in this work were obtained from MAST (Huang et al. 2020), hosted by the Space Telescope Science Institute (STScI). STScI is operated by the Association of Universities for Research in Astronomy, Inc., under NASA contract NAS 5-26555. This work also presents results from the European Space Agency (ESA) space mission Gaia. Gaia data are being processed by the Gaia Data Processing and Analysis Consortium (DPAC). Funding for the DPAC is provided by national institutions, in particular the institutions participating in the Gaia Multilateral Agreement. The Gaia mission website is https://www.cosmos.esa.int/web/gaia. The Gaia archive website is https://gea.esac.esa.int/archive/. This research has also made use of the VizieR catalog access tool, CDS, Strasbourg, France.

Table 5: Mode Visibilities[a]

ℓ	B	V	R	I
1	0.70930	0.70160	0.69360	0.68660
2	0.32490	0.31130	0.29710	0.28480
3	0.05868	0.04797	0.03668	0.02690
4	0.02688	0.02969	0.03267	0.03535
5	0.01167	0.00964	0.00750	0.00572
6	0.00802	0.00937	0.01085	0.01214
7	0.00410	0.00333	0.00258	0.00198
8	0.00351	0.00436	0.00521	0.00592
9	0.00186	0.00154	0.00121	0.00096
10	0.00194	0.00245	0.00297	0.00340
11	0.00102	0.00086	0.00070	0.00057
12	0.00116	0.00149	0.00184	0.00212
13	0.00058	0.00049	0.00041	0.00034
14	0.00080	0.00103	0.00127	0.00147
15	0.00041	0.00036	0.00031	0.00026

Notes. (a) Computed for the B, V, R, and I wavebands. The same values used to generate Figure 10.

References

Aerts C., Christensen-Dalsgaard J., Kurtz D. W., 2010, aste.book. doi:10.1007/978-1-4020-5803-5
Astropy Collaboration, Robitaille, T. P., Tollerud, E. J., et al. 2013, A&A, 558, A33
Astropy Collaboration, Price-Whelan, A. M., Sipöcz, B. M., et al. 2018, AJ, 156, 123
Astropy Collaboration, Price-Whelan, A. M., Lim, P. L., et al. 2022, ApJ, 935, 167
Bailer-Jones, C. A. L., Rybizki, J., Fouesneau, M., Demleitner., M., Andrae, R., 2021, AJ, 161, 147
Balona, L.A., Daszyńska-Daszkiewicz, J., & Pamyatnykh, A.A. 2015, MNRAS, 3073
Bianchi, L., Shiao, B., & Thilker, D. 2017, ApJS, 230, 24
Biró, I.B., & Nuspl, J., 2011, MNRAS 416, 1601
Rowman, D.M., Kurtz, D.W., Breger, M., Murphy, S., & Holdsworth, D.L. 2016, MNRAS, 460, 1970
Cardelli J. A., Clayton G. C., & Mathis J. S., 1989, ApJ, 345, 245
Carter, J., Rappaport, S., & Fabrycky, D. 2011, ApJ, 728, 139
Castelli F., Kurucz R. L., 2003, in IAU Symposium, Vol. 210, Modelling of Stellar Atmospheres, Piskunov N., Weiss W. W., Gray D. F., eds., p. A20
Çelik, E., Kahraman Aliçavuş, F. 2024, PASJ, 76, 787
Chambers, K.C., Magnier, E.A., Metcalfe, N., et al. 2016, arXiv:1612.05560
Choi J., Dotter A., Conroy C., Cantiello M., Paxton B., Johnson B. D., 2016, ApJ, 823, 102
Cowling, T.G. 1941, MNRAS, 101, 367
Cutri, R.M., Wright, E.L., Conrow, T., et al. 2013, wise.rept, 1C.
Danielski, C., Babusiaux, C., Ruiz-Dern, L., Sartoretti, P., & Arenou, F. 2018, A&A, 614, A19
Daszyńska-Daszkiewicz, J., Dziembowski, W.A., Pamyatnykh, A.A., & M.-J. Goupil, M.-J. 2002, A&A, 392, 151
Daszyńska-Daszkiewicz, J., Dziembowski, W.A., & Pamyatnykh, A.A. 2006, A&A, 77, 113
Di Mauro, M.P., Cardini, D., Catanzaro, G., et al. 2011, MNRAS 415, 3783
Dotter A., 2016, ApJS, 222, 8
Dziembowski, W. A., 1977, Acta Astr. 27, 203
Eddington A. S., 1919, MNRAS, 79, 171. doi:10.1093/mnras/79.3.177
Eddington A. S., 1919, MNRAS, 79, 177
Eddington A. S., 1926, ics..book
Feinstein, A.D., Montet, B.T., Foreman-Mackey, D., et al. 2019, PASP, 131, 94502
Fuller, J., Kurtz, D., Handler, G., & Rappaport, S. 2020, MNRAS, 498, 5730
Fuller, J., Rappaport, S., Jayaraman, R., Kurtz, D., & Handler, G. 2025, ApJ, 979, 80
Gamarova, A.Yu., Mkrtichian, D.E., Rodriguez, E., Costa, V., & Lopez-Gonzalez, M.J. 2003, ASPC 292, 369
Gunn, J.E., Carr, M., Rockosi, C., et al. 1998, AJ, 116, 3040
Handler, G., Kurtz, D.W., Rappaport, S.A., et al. 2020, NatAs, 4, 684
Handler, G., Rappaport, S., Jones, D., et al. 2025, A&A, 702, A104
Harris, C. R., Millman, K.J., van der Walt, S.J., et al. 2020, Nature, 585, 357
Huang, C. X. 2020, TESS Lightcurves From The MIT Quick-Look Pipeline ("QLP"), STScI/MAST, doi:10.17909/t9-r086-e880
Hunter, J. D. 2007, CSE, 9, 90

Jayaraman, R. Handler, G., Rappaport, S., Fuller, J., Kurtz, D.W., Charpinet, S., and Ricker, G.R. 2022, ApJL, 928, L14
Jayaraman, R., Rappaport, S. Powell, B., et al. 2024, ApJ, 975, 121
Jayaraman, R., et al. 2026, in preparation.
Johnston, C., Tkachenko, A., Van Reeth, T., Bowman, D. M., Pavlovski, K., Sana, H., & Sekaran, S. 2023, A&A 670, 167
Katz, D., Sartoretti, P., Guerrier, A., et al. 2023, A&A, 674, A5
Kjeldsen, H., Bedding, Butler, P., et al. 2005, ApJ, 635, 1281
Kopal, Z. 1959, Close Binary Systems, The International Astrophysics Series, London; Chapman & Hall
Kostov, V., Powell, B.P., Fornear, A.U., et al. 2025, ApJS, 279, 50
Kovács, G., Zucker, S., & Mazeh, T. 2002, A&A, 391, 369
Kunimoto, M., Huang, C., Tey, E., et al. 2021, Research Notes of the AAS, 5, 234
Kunimoto, M., Tey, E., Fong, W., et al. 2022, Research Notes of the AAS, 6, 236
Kurtz D. W., 1982, MNRAS, 200, 807. doi:10.1093/mnras/200.3.807
Kurtz, D.W., Handler, G., Rappaport, S., et al. 2020, MNRAS, 494, 5118
Kurtz, D.W. 2022, ARA&A, 60, 31
Mowlavi, N., Holl, B, Lecoeur-Taïbi, I., et al. 2023, A&A, 674, A16
Larson, T. & Schou, J. 2011, JPhCS, 271,12062
Larson, T.P., Schou, 2015, Sol Phys, 290, 3221
Lee, J. W., Hong, K., Park, J.-H., Wolf, M., Kim, D.-J. 2023, AJ, 165, 159
Lehmann, H., Dervişoğlu, A., Mkrtichian, D. E., Pertermann, F., Tkachenko, A., Tsymbal, V. 2020, A&A, 644, A121
Lenz, P., & Breger, M. 2005, Communications in Asteroseismology, 146, 53
Lightkurve Collaboration, Cardoso, J.V.d.M., Hedges, C., et al., 2018 Lightkurve: Kepler and TESS Time Series Analysis in Python, Astrophysics Source Code Library, ascl:1812.013
O'Connell, D.J.K. 1951, Riverview College Observatory Publications. 2 (6): 85. Bibcode:1951PRCO....2...85O
Ochsenbein, F., Bauer, P., & Marcout, J. 2000. A&AS, 143, 23
Paxton B., Bildsten L., Dotter A., Herwig F., Lesaffre P., Timmes F., 2011, ApJS, 192, 3
Paxton B. et al., 2015, ApJS, 220, 15
Paxton B., 2019, ApJS, 243, 10
Powell, B., Kostov, V., Rappaport, S., et al. 2021, AJ, 161, 162
Powell, B. 2026, private communication.
Prša, A., & Zwitter, T. 2005, ApJ, 628, 426
Rappaport, S., Kurtz, D.W., Handler, G., et al. 2021, MNRAS, 503, 254
Rappaport, S., Borkovits, T., Gagliano, R., et al. 2022, MNRAS, 513, 434
Reed, M.D., Brondel, B.J., & Kawaler, S.D. 2005, ApJ, 634, 602
Ricker, G.R., Winn, J.N., Vanderspek, R., et al. 2015, JATIS, 1, 14003
Scherrer, P. H., Schou, J., Bush, R. I., et al. 2012, SoPh, 275, 207
Shibahashi, H., & Kurtz, D.W. 2012, MNRAS, 422, 738
Skrutskie, M.F., Cutri, R.M., Stiening, R., et al. 2006, AJ, 131, 1163
Stassun, K.G., Oelkers, R.J., Paegert, M., et al. 2019, AJ, 158, 138
Stello, D., Cantiello, M., Fuller, J., et al. 2016, Nature 529, 364
Van Reeth, T., Johnston, C., Southworth, J., Fuller, J., Bowman, D.M., Poniatowski, L., Van Beeck, J. 2023, A&A, 671, A121
Virtanen, P., Gommers, R., Oliphant, T. E., et al. 2020, NatMe, 17, 261
Yakut, K., Kalomeni, B., & Rappaport, S. 2025a, MNRAS, 542, 1817
Yakut, K., Kalomeni, B., Rappaport, S., & Kostov V. 2025b, MNRAS, 544, 271
Yuan, J.-Zh., Qian, Sh.-B. 2019, Res. A&Ap, 19, 128
Zhang, V., Rappaport, S., Jayaraman, R., Kurtz, D., Handler, G., Fuller, J., & Borkovits, T. 2024, MNRAS, 528, 3378

Appendix A: Changes in the Pulsation Frequencies and the Orbital Period

Both the pulsation frequencies and the orbital period appear nearly constant across the 200-s cadence data from the four contiguous TESS sectors 63-66, or even to some extent when we include the final three sectors of 200-s cadence—separated from the former sectors by about 700 d. However, the apparently constant pulsation frequencies are seen to be clearly varying once we add five earlier sectors with 600-s cadence data (sectors between S30 and S39). Overall, after analyzing the available TESS data between sectors S30 and S93, the pulsation frequencies are all found to be significantly increasing with time. The orbital period can be tracked to even earlier times by using six sectors between S3 and S13 with 30-min cadence. The orbital frequency is also found to be increasing with time. We thus sought to characterize the frequency changes in the pulsations as well as in the orbit.

To track the pulsation phases ϕ (see also Bowman et al. 2016), we fit a sine curve of the form $A \cos[\omega(t - t_{\rm ecl}) - \phi]$ to represent a pulsation over an interval of, say, half of a full TESS sector (∼12 d). We needed to consider sufficiently long intervals because some of the pulsation peaks are within a fraction of 1 d^{-1} of other peaks. The reference time, $t_{\rm ecl}$ is the time of a primary eclipse, e.g., BJD 2460014.476. We then fit for A and ϕ and stepped the fitting window forward in time by a fraction of a TESS sector.

The results of tracking the phase for each of the 6 pulsation frequencies are given in Figure A.1. Each panel displays the equivalent Eclipse Timing Variation (ETV) curve for both components of a given pulsation mode: D1a and D1b, D2a and D2b (top two panels) and O1a and O1b in the lower left panel. Note that for mode D1, the a and b components track each other very well, and we saw in Fig. 4 that indeed these two components are always in phase at the primary eclipses. By contrast, we can see from the ETVs of D2 and O1 that the ETV curves for the two components are separated by close to half a pulsation period, consistent with the fact that the two components of both modes remain out of phase at the primary eclipses over all the sectors with 10-min or better cadence.

The final panel in Fig. A.1 shows the ETV curve for the orbital period. This shows that $P_{\rm orb}$ is also *apparently* decreasing with time. If we interpret this as an orbital decay, then the decay timescale of just $\sim 2 \times 10^5$ yr seems rather implausible. Alternatively, we might interpret the curve as a portion of a Doppler delay orbit caused by an orbiting third body. Unfortunately, the duration of available TESS data is insufficient to determine an outer orbit for a putative third body. However, for one of the shorter allowed orbits of 15 yr, the semi-major axis is 950 light-seconds (for an assumed circular orbit), and the corresponding mass function is $f(M) \simeq 0.03\,{\rm M}_\odot$. For a binary mass of $3\,{\rm M}_\odot$ (see Table 4), this yields a value of $M_3 \sin^3 i$ of about $0.75\,{\rm M}_\odot$. A third body of such a mass would not have contributed sufficient light to the SED to have been unequivocally detected, especially for outer inclination angles of $\gtrsim 75°$. We note that the known secondary in the binary contributes only $\lesssim 0.01$ of the system luminosity, and a comparable third star would barely perturb the SED.

Table A.1: Summary Of Frequencies and Frequency Derivatives in TIC 287869463[a]

ν d^{-1}	$\nu_{\rm split}$[b] d^{-1}	$\dot\nu$[c] 10^{-6} d^{-2}	diff. in $\dot\nu$ $10^{-8} d^{-2}$
38.45620(1)	0.727516(20) ×2	0.90(4)	7(6)
39.91123(1)	0.727516(20) ×2	0.97(4)	7(6)
36.36627(2)	0.727514(34) ×2	3.15(8)	7(11)
37.82130(2)	0.727514(34) ×2	3.28(8)	7(11)
34.94617(3)	0.727518(39) ×6	2.47(9)	18(12)
39.31127(3)	0.727518(39) ×6	2.65(9)	18(12)

Notes. (a) All frequencies are referenced to an epoch of BJD 2460000. Values in parentheses are the uncertainties in the last digits. (b) For reference, the orbital frequency at the same epoch is 0.727,518,2(1) d^{-1} or $P_{\rm orb}$ = 1.374,536,0(2). (c) For reference, $\dot\nu_{\rm orb} \simeq 0.009$ in the same units.

Returning to the systematic non-linear behavior in the ETV curves for the pulsations, we examine what the consequences would be for different assumptions about the nature of the non-linear ETV curve observed for the orbit. Suppose that a Fuller mode pulsation frequency is $\nu_{\rm p}$, and that it is *physically* changing with time as $\dot\nu_{\rm p}$. The splitting with the orbit will be $\pm m\,\nu_{\rm orb}$ (see, e.g., Shibahashi & Kurtz 2012). Now, we also allow that the orbital frequency is *physically* changing as $\dot\nu_{\rm orb}$. This means that the two components of the mode ("upper" and "lower") should follow different functions of time:

$$\nu_{\rm p,u} = \nu_{\rm p} + m\,\nu_{\rm orb} + \dot\nu_{\rm p} t + m\,\dot\nu_{\rm orb} t \quad (A.1)$$

$$\nu_{\rm p,l} = \nu_{\rm p} - m\,\nu_{\rm orb} + \dot\nu_{\rm p} t - m\,\dot\nu_{\rm orb} t \quad (A.2)$$

In turn, if we were to measure the $\dot\nu_{\rm p}$ of the upper and lower components, we should find

$$\dot\nu_{\rm p,u} = \dot\nu_{\rm p} + m\,\dot\nu_{\rm orb} \quad (A.3)$$

$$\dot\nu_{\rm p,l} = \dot\nu_{\rm p} - m\,\dot\nu_{\rm orb} \quad (A.4)$$

with a difference in $\dot\nu_{\rm p}$ of $2m\,\dot\nu_{\rm orb}$. From Table A.1 we can see that the differences between the $\dot\nu$ terms of the upper and lower frequency components are not statistically significant, and the uncertainties are $\sim 10^{-7}$ d^{-2}. For the octupole mode, we might expect a change in the difference of the $\dot\nu$'s by about $6 \times 9 \times 10^{-9} = 5.4 \times 10^{-8}$ d^{-2} due to the changing orbit. This is smaller than the uncertainty in the difference in $\dot\nu$ listed in Table A.1 for the octupole mode. Thus, we cannot use this effect to test for a decaying orbit.

For Doppler shifts of the binary (which include the pulsating star) the quantity $\dot\nu/\nu$ would be constant. So, we should find that all the pulsation components have $\dot\nu_{\rm p}/\nu_{\rm p} = \dot\nu_{\rm orb}/\nu_{\rm orb}$, or $\dot\nu_{\rm p} \simeq 50\,\dot\nu_{\rm orb} \simeq 0.5 \times 10^{-6}$ d^{-2}. In all cases, this is less than the values of $\dot\nu$

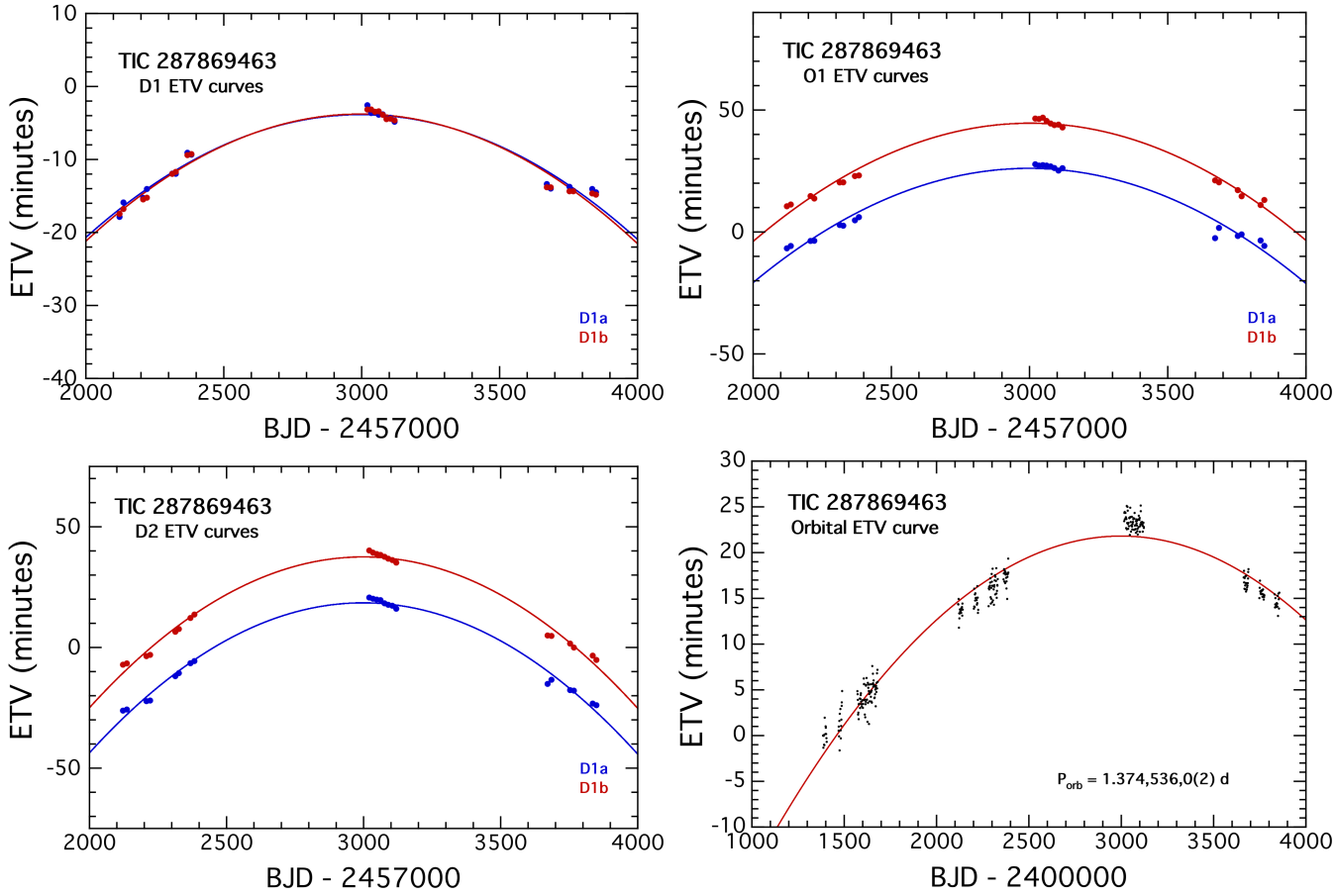

Fig. A.1: ETV curves for each component of the three pulsation modes, D1, D2, and O1, as well as from the binary orbital period. All four curves show decreasing periods with time, but not at the same rates. All phases are referenced to the times of a primary eclipse, i.e., at BJD - 2,456,014.4757. Note that the vertical scale for the D1 ETVs is exactly 1/3 that for the D2 and O1 ETVs. In turn, the vertical scale for the orbital ETV curve is 3/5 that of the D1 ETVs.

for the pulsations listed in Table A.1, but would be readily detectable if we could separate the Doppler and other natural changes in pulse frequency.

Regarding the observed (or apparent) changes in the orbital ETV curve, we point out that many such close binaries containing an early-type star exhibit ETVs that have non-linear variations on long timescales (decades or even centuries) that are almost certainly neither actual orbital period changes (i.e., orbital decay) nor third-body induced light travel-time effects. Some examples of very irregular and unexplained ETVs are the cases of XZ And (Yuan & Qian 2019), X Tri (Lee et al. 2023), RZ Cas (Lehmann et al. 2020), and Y Cam (Çelik & Kahraman Aliçavuş 2024). While we are confident in the non-linear behavior of the TIC 287869463 ETV curve, we cannot be certain what causes this behavior. Therefore, at least tentatively, we take all the $\dot{\nu}$'s for the pulsations to be independent of the orbit, and for the orbital $\dot{\nu}_{\rm orb}$ to be due to neither an orbital decay nor an orbital Doppler shift.